High-Performance Computational Modeling of Plasma-Surface Interactions and RF Antennas

T. G. Jenkins[1] and D. N. Smithe[1]

[1]Tech-X Corporation, 5621 Arapahoe Avenue Suite A, Boulder, CO 80303, USA

Corresponding Author: tgjenkins@txcorp.com

Abstract:

The heating of confined tokamak plasma to fusion-relevant temperatures can cause sputtering of high-Z impurities from plasma-facing components, and such impurities radiatively cool the plasma, especially as transport effects carry them to the reactor core. The sputtering process is believed to be exacerbated by the large electromagnetic fields generated by RF antennas, since these fields alter the dynamics of sheaths that form on antenna components in contact with plasma. Recent advances in finite-difference time-domain (FDTD) modeling techniques enable the physics of localized sheath potentials to be modeled concurrently with the physics of antenna near- and far-field behavior and RF power flow. When implemented on high-performance computing platforms, such techniques enable the study of plasma-surface interactions in realistic experimental ion-cyclotron resonance heating scenarios at previously inaccessible levels of resolution. We present results from high-performance (10k–100k core) FDTD simulations of Alcator C-Mod's field-aligned ICRF antenna, considering (a) sputtering and impurity production, as driven by self-consistent sheath potentials at antenna surfaces, and (b) the physics of slow wave excitation in the immediate vicinity of the antenna hardware and in the scrape-off layer for various edge densities. To our knowledge, these half-torus models constitute the most advanced time-domain simulation capabilities that have yet been developed for the study of ICRF-induced wave physics and plasma-material interactions in realistic experimental geometries.

1 Introduction

In magnetically confined fusion plasma, physical processes occurring in the plasma edge and scrape-off layer (SOL) can reduce the effectiveness of the RF sources used to drive current within, or to heat, the core plasma. Parametric decay instabilities or other resonant phenomena may be excited in the plasma edge; these parasitically divert portions of the injected RF power from its desired destination and reduce RF antenna efficiency. In addition, sheath formation on plasma-facing antenna components may induce sputtering of high-Z ions from these surfaces, and the radiative cooling that such impurity components induce as transport processes carry them toward the reactor core may quench the

fusion reaction altogether. The plasma edge density plays a significant role in these interactions. Higher densities near plasma-facing antenna components are associated with higher sheath potential drops and higher material sputtering rates, and although reduced densities and sheath potential values can be achieved by widening the gap between the antenna and the plasma's last closed flux surface, such a change may also open additional, undesired channels into which RF wave power may flow.

In this paper, we describe numerical techniques for modeling parasitic wave excitation and plasma-material interaction physics in the tokamak edge and scrape-off layer. We will demonstrate that the evolution of RF wave fields and sheath potentials can be self-consistently modeled in the finite-difference time-domain (FDTD) formalism, using realistic experimental configurations and plasma profiles. Half-torus simulations of ICRF heating in the Alcator C-Mod tokamak, resolved spatially at the sub-millimeter level and running for tens to hundreds of ICRF periods, will be described; we will also discuss a process for modeling sputtering impurity generation in these discharges. Complex numerical simulations such as these are possible only due to the increasing capabilities afforded by massively parallel supercomputing platforms, and the computations we describe here exercise these capabilities at large scales (tens to hundreds of thousands of processor cores) to model RF antenna operation at unprecedented levels of detail.

2 Modeling ICRF physics in the time domain

This section discusses various techniques used to incorporate realistic machine geometries, material properties, and plasma profiles into the VSim code [1] to produce the 3D half-torus numerical model used in this work.

2.1 Electromagnetic FDTD Methods

VSim uses a modified electromagnetic finite-difference time-domain (FDTD) method [2]. As is the case with conventional FDTD methods, the electric and magnetic field vector components associated with an individual grid cell are not co-located at the cell nodes, but are evaluated (respectively) on edges and faces of the grid cell. Leap-frog time-staggering of the electric and magnetic fields relative to one another preserves proper time-centering; the path and surface integrals of Maxwell's equations are evaluated respectively around cell edges and over cell faces to center these equations properly in space. Cold-plasma currents in the Maxwell equations can also be included in the FDTD formalism [3], provided that the components of plasma current associated with an individual grid cell are co-located at cell nodes [permitting concurrent evaluation of the cold-plasma evolution equation (3); see below]. Interpolation methods which carry edge fields to the grid nodes ("edge-to-node") and nodal fields to edges ("node-to-edge") become necessary when such sources are used. Reference [3] also describes the formulation of a locally implicit time-advance algorithm for the plasma sources, enabling the numerical restrictions imposed by plasma cutoffs (when wave phase velocities diverge) to be circumvented and preserving the physics of linear plasma dispersion in the presence of a background magnetic field.

Cut-cell techniques [4] can be used to model geometrically complex boundaries in the FDTD formalism. Cut edge lengths, associated with portions of individual grid cells intercepted by and lying partially outside conducting boundaries, are used in the integral Maxwell equations. Edge-to-node and node-to-edge operations for the corresponding fields must be appropriately modified to reflect the presence of the conducting boundary. At this boundary, the physics of plasma sheath formation can also be modeled. Because of the extreme length scale disparity between the width of such sheaths (generally a few Debye lengths) and the wavelength of the ICRF wave phenomena of interest here, direct spatial resolution of the sheath is computationally prohibitive for realistic 3D antenna structures. However, one can model its effects through the use of a "sub-grid sheath boundary condition", in which local capacitive and resistive circuit elements associated with the presence of the sheath are defined at the nodes of grid cells intersecting the material boundary [5], enabling a local sheath potential to be defined at this boundary. Reference [6] generalizes the methods of Ref. [3], and describes how to model time-varying sheath potentials at the conducting boundary without spatially resolving the sheath. In this work, fields at the n-th simulation timestep Δt are evolved to the $(n+1)$-st timestep by the equations

$$\frac{\mathbf{B}^{n+1/2}-\mathbf{B}^{n}}{(\Delta t/2)} = -\nabla\times(\mathbf{M}^{T}\cdot\mathbf{e}^{n}) \quad \text{(explicit, half-Faraday)} \tag{1}$$

$$\frac{\mathbf{e}^{n+1}-\mathbf{e}^{n}}{\Delta t} = -\frac{1}{\epsilon_0}\sum_{\alpha}\left(\frac{\mathbf{j}_{\alpha}^{n+1}+\mathbf{j}_{\alpha}^{n}}{2}\right)+c^{2}\mathbf{M}\cdot(\nabla\times\mathbf{B}^{n+1/2}) \quad \text{(implicit, Ampere)} \tag{2}$$

$$\frac{\mathbf{j}_{\alpha}^{n+1}-\mathbf{j}_{\alpha}^{n}}{\Delta t}+\Omega_{\alpha}\times\left(\frac{\mathbf{j}_{\alpha}^{n+1}+\mathbf{j}_{\alpha}^{n}}{2}\right) = \epsilon_0\omega_{p\alpha}^{2}\left[\left(\frac{\mathbf{e}^{n+1}+\mathbf{e}^{n}}{2}\right)+\frac{\hat{n}}{\Delta_s}\left(\frac{\phi^{n+1}+\phi^{n}}{2}\right)\right] \quad \text{(implicit, current)} \tag{3}$$

$$\frac{\phi^{n+1}-\phi^{n}}{\Delta t} = -\frac{\Delta_s}{\epsilon_0}\hat{n}\cdot\sum_{\alpha}\left(\frac{\mathbf{j}_{\alpha}^{n+1}+\mathbf{j}_{\alpha}^{n}}{2}\right)-\nu_s\left(\frac{\phi^{n+1}+\phi^{n}}{2}\right) \quad \text{(implicit, sheath potential)} \tag{4}$$

$$\frac{\mathbf{B}^{n+1}-\mathbf{B}^{n+1/2}}{(\Delta t/2)} = -\nabla\times(\mathbf{M}^{T}\cdot\mathbf{e}^{n+1})\ . \quad \text{(explicit, half-Faraday)} \tag{5}$$

Here, $\mathbf{B}$ is the face-centered magnetic field, $\mathbf{e}$ is the node-centered electric field (obtained by applying the edge-to-node operator $\mathbf{M}$ to the edge electric field $\mathbf{E}$), $\mathbf{j}_\alpha$ is the plasma current of species α, and ϕ is the local sheath potential; Ω_α is the signed gyrofrequency of species α in the background magnetic field. Node-to-edge mappings are carried out by the transposed edge-to-node operator $\mathbf{M}^T$. Sheath potentials are defined only on grid nodes whose adjoining edges are cut by the conducting boundary; vectors normal to this boundary are interpolated to the neighboring nodes outside the boundary to form the unit normal $\hat{n}$ associated with each such node. The sheath width Δ_s and the dissipation parameter ν_s are, most generally, spatially and temporally varying numerical parameters defined on these boundary nodes. Equation (4) can be derived by considering Kirchhoff relations for the potential drop across a parallel RC circuit; the standard parallel-plate

capacitor relation $C = \epsilon_0 A/d$ (with A the cross-sectional plate area and d the plate separation) is generalized such that the plate separation corresponds with the time-varying sheath width Δ_s. The effective resistance $R = \eta\Delta_s/A$, proportional to the resistivity η and the inverse of area A, can be combined with the capacitance to form an effective time constant $\nu_s^{-1} = RC$ which is independent of both Δ_s and A. The use of current-per-unit area $\mathbf{J}$, rather than the total current I conventional in circuit equations, removes the dependence on A from the computation altogether. Equation (3), which computes the cold-plasma response of the species plasma currents $\mathbf{j}_\alpha$, removes the sheath electric field (subtracting the approximate negative gradient of ϕ across the thin layer Δ_s) to compute this response only as a function of the electromagnetic fields in the bulk plasma.

Explicit FDTD PIC simulations were used in Ref. [6] to quantify the circuit-like behaviors of the sheath. For these simulations, resistive effects were neglected, and a modified expression for the sheath width (compare with Ref. [5])

$$\Delta_s = \lambda_{De}\left[1 + \left(\frac{0.6 q_i \langle\phi(t)\rangle}{T_e}\right)^2\right]^{3/8} \tag{6}$$

was found to be valid for the cases considered. In Eq. (6), T_e and λ_{De} are the electron temperature and Debye length, q_i the elementary charge, and the averaging operation $\langle\ldots\rangle$ is over the RF wave period. This expression recovers the approximate Debye screening imparted by the DC sheath when sheath potentials are negligible, as well as the approximate Child-Langmuir behavior when these potentials are large. More detailed expressions for the sheath capacitance and resistance can also be incorporated into the model, and future code development efforts to incorporate such models (see, e.g., Ref. [7]) are envisioned.

2.2 Simulation geometry

Simulations are carried out on a rectangular mesh encompassing half of the Alcator C-Mod torus. Beginning with an initially metal-filled domain; toroidally symmetric boundary wall data (see black curve in Fig. 1a) is read from an equilibrium EQDSK file and rotated to hollow out the 3D vacuum vessel interior. Limiter boundaries corresponding to antenna surfaces are ignored in this data; the approximate shape of the interior vessel is shown in the red curve of Fig. 1a. The CAD file for C-Mod's field-aligned ICRF antenna (Fig. 1b) is then imported into the simulation and properly aligned with the axisymmetric wall, in conjunction with the hollowing out of an appropriately-sized vacuum region in which the antenna will reside. Portions of the coaxial antenna feeds that extend outside the rectangular simulation domain are neglected; current driven within the remaining portions of the feeds powers the antenna. A midplane cross-section of the simulation domain is shown in Fig. 1c, including portions of the coaxial feeds (top middle), antenna hardware (top), inboard and outboard vessel walls, and the plasma's last closed flux surface; the full simulation domain generalizes this figure to a 3D region extending into and out of the page (see Fig. 2c). Open boundary conditions are used on the non-metal-filled boundaries of the coaxial feeds, while a matched absorbing layer boundary condition is used on the non-metallic portions of the plane bisecting the torus (the bottom of Fig.

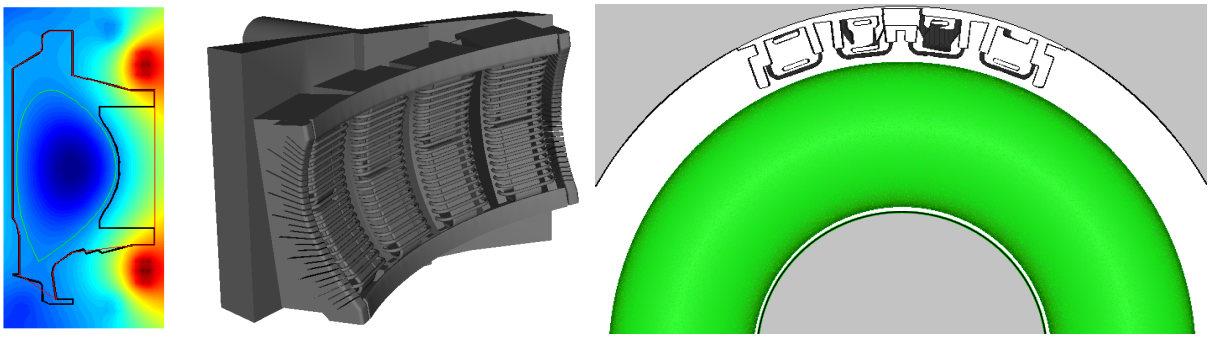

FIG. 1: [a] Equilibrium EQDSK data from Alcator C-Mod used to construct the simulation geometry. The approximate axisymmetric shape of the vacuum vessel (red curve) is constructed from the EQDSK limiter data (black curve), ignoring contributions from the toroidally asymmetric antenna. Magnetic flux (background) and separatrix (green curve) are also shown. [b] 3D CAD rendering of C-Mod's field-aligned ICRF antenna, as imported into the simulation. [c] Midplane cut of the 3D simulation domain, showing antenna hardware (top), inboard/outboard vessel walls, and the plasma domain (green region). Regions outside the vessel (top left/right, bottom middle) are metal-filled.

1c). The remaining boundaries of the simulation domain are metallic (Fig. 1c does not show the full extent of the domain from left to right).

2.3 Plasma and Field Profiles

The magnetic fields which confine the plasma are constructed from the EQDSK file. Bicubic spline interpolation is used to interpolate magnetic flux values from the 2D EQDSK representation to the 3D simulation grid. For the plasma density profile, Thomson scattering data from the outboard midplane in C-Mod shot 1050426022 (Fig. 2a) is fitted to a smooth curve; corresponding flux values from the midplane are then used to interpolate this density over the simulation domain (Fig. 2b). No profile data for the scrape-off layer was obtained for this shot; we have constructed an exponentially decaying profile of variable width (maintaining C^1 continuity with the curve of Fig. 1a) to represent the density outside the last closed flux surface. Variation of this profile enables us to study the relationship between SOL density and slow wave excitation.

2.4 Material properties and sputtering

The physics of sputtering is sensitive to the material surface composition, and the simulation model must therefore represent the different surfaces which comprise the antenna and vacuum vessel as separate objects. Protective tiling on C-Mod's interior vessel surfaces is made of TZM (a molybdenum alloy with traces of titanium, zirconium, and carbon). The antenna straps (copper, in Fig. 3a) and limiter structures (grey notched structures surrounding the straps) are high-purity oxygen-free copper plated respectively over elec-

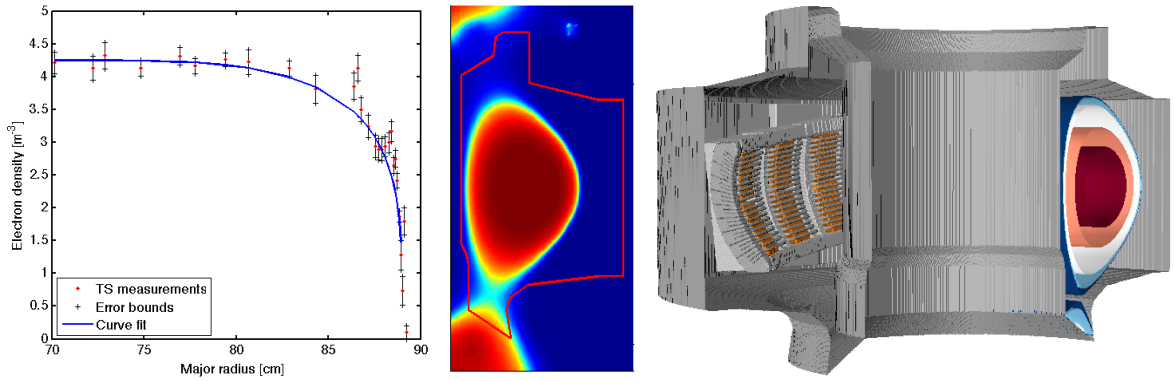

FIG. 2: [a] Thomson scattering data for electron density in C-Mod shot 1050426022, with error bars and curve fit. No measurements in the scrape-off layer were obtained for this shot. [b] Interpolation of the electron density data to the 2D EQDSK grid (only densities inside the closed red curve are used). [c] Simulation domain in its entirety, including the antenna, vacuum vessel, and contours of plasma density interpolated to the 3D simulation grid. Plasma contours are cut away at the left for ease of visualization.

troless nickel flash on Inconel 625 and 316 stainless steel. Faraday shields (horizontal rods in front of antenna straps) are also made of TZM. Importing these different antenna and wall components as separate objects, each with its own material properties, facilitates accurate sputtering yield computations.

3 Initial Results: Sputtering and ICRF Wave Physics

Test particles, which respond to the electromagnetic fields of the RF waves but do not contribute to these fields, are loaded into the simulation with spatial profiles matching the plasma's edge and SOL profiles. Temperature profiles for these particle distributions are also obtained from C-Mod data (not shown). As the simulation proceeds, particles which pass through the sheath to strike the material wall have their strike energy modified in accordance with the local sheath potential at the strikepoint, enabling the sputtering computations to accurately take into account the energetics of sheath transit. We continue to develop the model's sputtering capabilities; current areas of focus include improving ionization models in the SOL for the sputtered neutral wall atoms, as well as improving surface models for the material alloys comprising the wall and antenna surfaces. Figure 3b shows initial data from the sputtering modeling; here, the ICRF antenna was run for many RF periods to determine the locations on the antenna where ion strikepoints were most likely to occur. The relatively few sputtering events on the upper right and lower left antenna housings, relative to other locations on the housing and the Faraday shields, is an issue of some curiosity. We are exploring the possibility that such time-integrated data can be compared with wear/erosion patterns on C-Mod antenna structures. In addition, we hope to apply the model to more generally explore sputtering impurity production,

impurity transport, and the interaction of RF waves with impurity populations.

Figure 4 shows initial data from ICRF wave modeling in Alcator C-Mod. In this discharge adjacent antenna straps are driven 180° out of phase from one another, yielding complex wave patterns as fast waves are excited in the edge plasma and propagate toward the plasma core (contours in the figure show oppositely signed values of the vertical electric field). In addition to the fast waves, slow wave excitations in the plasma edge and SOL are visible in the simulations. Current modeling efforts are focusing on the fate of the power which flows from the antenna and is diverted into these slow waves; quantifying the power losses associated with parasitic slow wave excitations as plasma edge parameters are varied will enable more efficient antenna operation scenarios to be developed.

4 Acknowledgements

This work is supported by the U.S. Department of Energy (DoE), Office of Science, OFES, under Award Numbers DE-FC02-08ER54953 and DE-SC0009501. This research used resources of the Oak Ridge Leadership Computing Facility at the Oak Ridge National Laboratory, which is supported by the Office of Science of the U.S. DoE under Contract No. DE-AC05-00OR22725. We thank Steve Wukitch, Paul Bonoli, and Yijun Lin (MIT-PSFC) for providing data and useful details about the C-Mod experiments. Animations of the simulations discussed here are available at `https://nucleus.txcorp.com/~tgjenkins/movies.html`.

References

[1] NIETER, C., CARY, J. R., "VORPAL: a versatile plasma simulation code", J. Comp. Phys. 196 (2004) 448. See also https://txcorp.com/vsim.

[2] YEE, K. S., "Numerical solution of initial boundary value problems involving Maxwell's equations in isotropic media", IEEE Trans. Anten. Prop. 14 (1966) 302.

[3] SMITHE, D. N., "Finite-difference time-domain simulation of fusion plasmas at radiofrequency time scales", Phys. Plasmas 14 (2007) 056104.

[4] DEY, S., MITTRA, R., "A locally conformal finite-difference time-domain (FDTD) algorithm for modeling three-dimensional perfectly conducting objects", IEEE Microw. Guided Wave Lett. 7 (1997) 273.

[5] D'IPPOLITO, D. A., MYRA, J. R., "A radio-frequency sheath boundary condition and its effect on slow wave propagation", Phys. Plasmas 13 (2006) 102508.

[6] JENKINS, T. G., SMITHE, D. N., "Benchmarking sheath subgrid boundary conditions for macroscopic-scale simulations", Plas. Sources Sci. Tech. 24 (2015) 015020.

[7] MYRA, J. R., D'IPPOLITO, D. A., "Radio frequency sheaths in an oblique magnetic field", Phys. Plasmas 22 (2015) 062507.

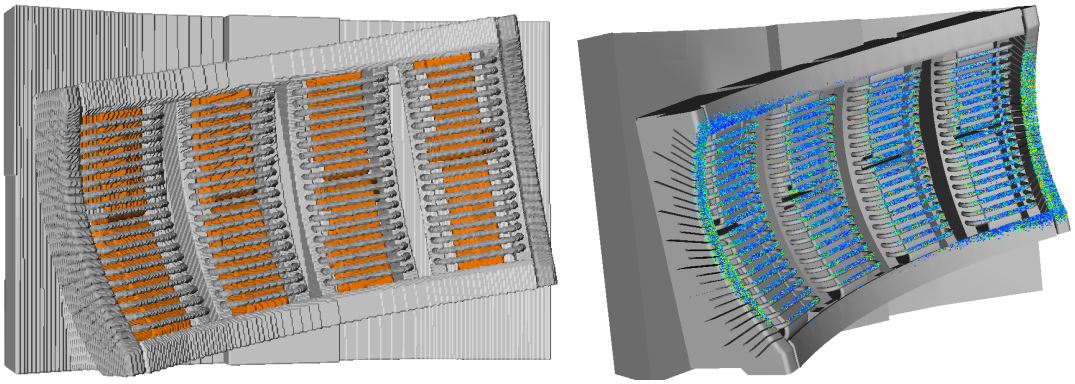

FIG. 3: [a] Close-up of the C-Mod ICRF antenna showing the different material composition of antenna components (copper straps, bounded in front by TZM Faraday shields and on the sides by copper-plated stainless steel). [b] Sputtering sites arising from test-particle collisions with antenna surfaces, shown over many RF cycles (darker colors represent strikes occurring earlier in the discharge).

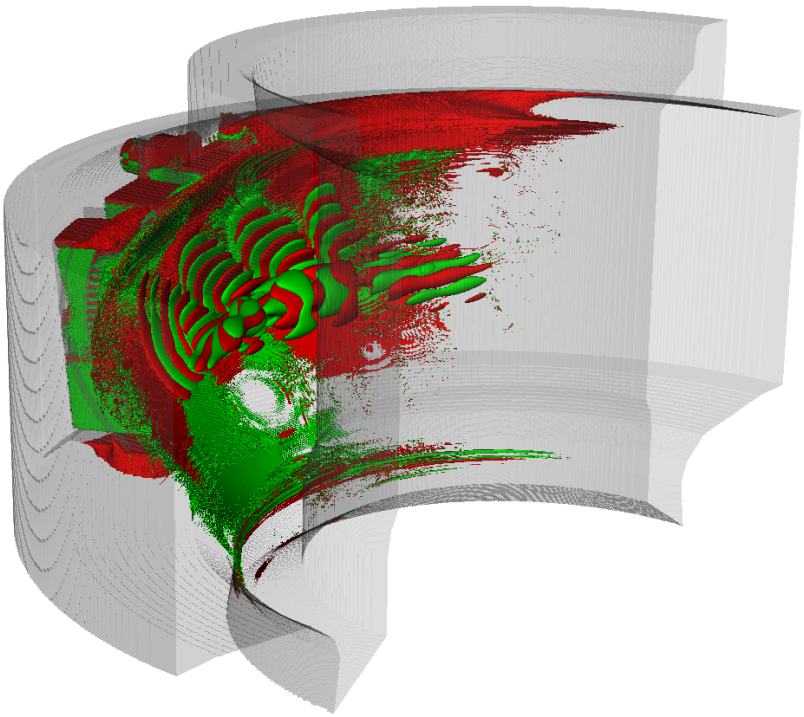

FIG. 4: VSim modeling of ICRF antenna operation in Alcator C-Mod; contours of vertical electric field (red/green contours have equal magnitudes and opposite signs) are shown. Fast waves induced by the antenna generate periodic wave structures near the tokamak core; some power is lost in the SOL as slow waves are excited in the thin layer below the density cutoff. This simulation used 60,000 HPC cores on the Titan Cray XK7, simulating 250 RF antenna periods at sub-millimeter spatial resolution in 12 wallclock hours.